


Upper limits of water contents in olivine and orthopyroxene of equilibrated chondrites and several achondrites

Dennis HARRIES ^{1,2*}, Xuchao ZHAO ³, and Ian FRANCHI ³

¹Department of Analytical Mineralogy, Institute of Geoscience, Friedrich Schiller University Jena, Carl-Zeiss-Promenade 10, 07745 Jena, Germany

²European Space Resources Innovation Centre, Luxembourg Institute of Science and Technology, 41 rue du Brill, L-4422 Belvaux, Luxembourg

³School of Physical Sciences, The Open University, Walton Hall, Milton Keynes MK7 6AA, UK

*Corresponding author.

Dennis Harries, Department of Analytical Mineralogy, Institute of Geoscience, Friedrich Schiller University Jena, Carl-Zeiss-Promenade 10, 07745 Jena, Germany.

E-mail: dennis.harries@esric.lu

(Received 11 June 2022; revision accepted 21 March 2023)

Abstract—Hydroxyl defects in nominally anhydrous minerals (NAMs) were potential carriers of water in the early Solar System and might have contributed to the accretion of terrestrial water. To better understand this, we have conducted a nanoscale secondary ion mass spectrometry survey of water contents in olivine and orthopyroxene from a set of equilibrated ordinary chondrites of the L and LL groups (Bazskówka, Bensour, Kheneg Ljouâd, and Tuxtuac) and several ultramafic achondrites (Zakłodzie, Dhofar 125, Northwest Africa [NWA] 4969, NWA 6693, and NWA 7317). For calibration, we used terrestrial olivine and orthopyroxene with H₂O contents determined by Fourier transform infrared. Our 99.7% (~3SD) detection limits are 3.6–5.4 ppmw H₂O for olivine and 7.7–10.9 ppmw H₂O for orthopyroxene. None of the meteoritic samples studied consistently shows water contents above the detection limits. A few exceptions slightly above the detection limits are suspected of terrestrial contamination by ferric oxyhydroxides. If the meteorite samples investigated accreted in the presence of small amounts of water ice, the upper limits of water contents provided by our survey suggest that the retention of hydrogen during thermal metamorphism and differentiation was ineffective. We suggest that loss occurred through combinations of low internal pressures, high permeability along grain boundaries, and speciation of hydrogen into reduced compounds such as H₂ and methane, which are less soluble in NAMs than in water.

INTRODUCTION

The delivery of water to the terrestrial planets is a long-standing problem in the understanding of planet formation in the early Solar System. Multiple isotopic anomalies point to a pronounced dichotomy of materials between the trans-Jupiter region harboring relatively oxidized, water-rich chondritic lithologies (carbonaceous chondrite [CC]-like isotopic compositions) and the inner Solar System characterized by mostly reduced, water-poor chondritic lithologies (non-carbonaceous [NC]-like isotopic compositions; Warren, 2011). These distinct reservoirs have preserved isotopic fingerprints that can be traced

through the melting and differentiation of early formed planetesimals that produced iron meteorites and achondrites.

Following hydrogen-isotopic constraints and astrophysical n-body models, hydrous CCs appear to be the best candidates for the inward transport of water by dynamical scattering during the late migration of Jupiter and Saturn into their current positions (Alexander et al., 2018; Raymond & Morbidelli, 2014; Walsh et al., 2011). Earth's bulk composition appears to be reasonably explained by the accretion of dominantly NC-like materials such as ordinary and enstatite chondrites, with the addition of a few percent to >10% of CC-like material (Dauphas, 2017; Rubie et al., 2015; Warren, 2011). Many

of the accreting bodies had diameters on the order of several 100 km, and most of them probably underwent early metamorphism, melting, and differentiation due to radiogenic heat (Morbidelli et al., 2009; Rubie et al., 2011).

Primitive, non-metamorphic/non-melted NC-like materials such as the ordinary chondrites of petrologic type 3 show ample evidence for the presence of aqueous to hydrothermal alteration (Alexander et al., 1989; Doyle et al., 2015; Grossman et al., 2000; Hutchison et al., 1987), suggesting that the materials of the NC-like region accreted small amounts of water ice or other hydrogen-bearing species. This poses an important question: Did NC- and CC-like planetesimals preserve hydrogen during metamorphism and melting and could they have delivered it efficiently to planets? Hydrogen and equivalent water contents present in nominally anhydrous minerals (NAMs) are of particular interest to study this question. Hydrogen in ferromagnesian silicate NAMs is mainly present as hydroxyl (OH) point defects in place of structural oxygen, which are charge compensated by tetrahedral (Si) and octahedral (Mg, Fe) vacancies (e.g., Lemaire et al., 2004; Stalder & Ludwig, 2007). Such structurally bound hydrogen is commonly expressed as a chemical component equivalent to H₂O, which we use also here to express hydrogen content. Terrestrial mantle peridotites frequently contain tens to hundreds of parts per million by weight (ppmw) of H₂O as hydroxyl groups in olivine and pyroxenes (e.g., Peslier, 2010). Molecular H₂O and H₂ are uncommon hydrogen carriers in NAMs, although the latter may be incorporated at high pressure under reducing conditions (Moine et al., 2020; Yang et al., 2016).

Samples of thermally metamorphosed ordinary chondrite material recovered from asteroid 25143 Itokawa seem to have formed in the presence of a methane-rich fluid phase (Harries & Langenhorst, 2018) and appear to preserve several hundred ppmw H₂O in NAMs (Chan et al., 2021; Jin & Bose, 2019). Jin and Bose (2019) and Jin et al. (2021) also report several hundred ppmw H₂O in pyroxenes of several Antarctic LL and L equilibrated ordinary chondrites and in pyroxenes of the chondrite falls, Chelyabinsk (LL5) and Benenitra (L6), leading them to infer minimal water loss during thermal metamorphism of inner solar system bodies and a lesser contribution of volatiles from larger heliocentric distances during the late accretion of terrestrial planets. Piani et al. (2020) report large bulk hydrogen contents of metamorphic EH4, EH5, and EL6 enstatite chondrites and igneous aubrites, reaching several thousand ppmw H₂O equivalent, of which a significant fraction may be incorporated into enstatite. Such amounts of hydrogen in the potential main building blocks of the terrestrial planets may have provided substantial amounts of their currently remaining water inventories.

To better understand the bound H₂O contents in NAMs of metamorphic chondrites and primitive and evolved achondrites, we conducted a survey of a diverse set of nine meteorite samples (plus two reference meteorites treated as blanks) and attempted to quantify trace hydrogen contents in olivine and orthopyroxene grains using a nanoscale secondary ion mass spectrometry (NanoSIMS).

SAMPLES AND METHODS

Reference Samples

We obtained several reference samples of mostly terrestrial olivine and orthopyroxene to serve as calibration standards for NanoSIMS analysis after quantification of their H₂O contents by Fourier transform infrared (FT-IR) spectroscopy. We included olivine from Sapat, Pakistan (Ol2536-1; Fa_{6.6±0.2}), olivine from Mogok, Burma (Ol24355-1; Fa_{8.3±0.2}), olivine of the Jepara pallasite (~Fa₁₂₋₁₃), orthopyroxene from Mogok (En24345-1; Fs_{7.9±0.2}Wo_{1.1±0.2}, 1.5 ± 0.2 mole% Al₂O₃), and orthopyroxene from Kilosa, Tanzania (En206269-1, two samples of the same crystal; Fs_{9.4±0.2}Wo_{0.4±0.1}). The crystal slabs were prepared as described below and studied by scanning electron microscopy (SEM) with energy dispersive X-ray spectroscopy. Backscattered electron imaging indicated no zoning or heterogeneities of major elements at the percent level. An additional olivine reference sample from San Carlos, Arizona/USA (~Fa₈₋₁₂) was available on two separate OU indium mounts.

We included the Neuschwanstein enstatite chondrite to serve as a near-blank reference sample for enstatite, because we expected very low contents of water due to the highly reduced mineralogy. Neuschwanstein is an EL6 chondrite (fall April 2002; Zipfel et al., 2010) and represents a thermally metamorphosed and extremely reduced mineralogy containing nearly Fe-free orthopyroxene (Fs_{1.8}), albitic plagioclase, Si-bearing kamacite, troilite, graphite, and oldhamite. The sample used stems from the second mass found and was extracted from the interior of the meteorite (sample E2) showing no iron oxyhydroxides staining.

Analyzed Meteorite Samples

The meteorite samples for this survey were chosen to represent a diverse range of planetary materials with an emphasis on thermally metamorphosed chondrites and achondrites suspected of having potentially elevated water contents in NAMs (FeO-rich and/or metal-poor lithologies). They comprise the following meteorites (Table 1):

TABLE 1. Petrological characteristics of the meteorite samples studied.

Sample	Fall/find	Type	Shock stage	Weathering grade
Baszkówka	Fall 1994	L5	S1	W0
Bensour	Fall 2002	LL6	S3	W0
Kheneg Ljouâd	Fall 2017	LL5/6	S3	W0
Tuxtuac	Fall 1975	LL5	S2	W0/1
Zakødzie	Find	UNGR	n.a.	Mod
Dhofar 125	Find	ACAP	S1	W1/2
NWA 5480	Find	Ol-DIO	Low	Low
NWA 4969	Find	BRA	Mod	Low
NWA 6693	Find	UNGR	S1	Low
NWA 7317	Find	CR6	S2	W0/1
Neuschwanstein	Fall 2002	EL6	S2	W0

Ordinary chondrites: Baszkówka is an equilibrated ordinary chondrite (L5, fall August 1994; Figure S6A) with remarkable macroporosity and euhedral silicate crystals, which have been linked to the presence of a volumetrically significant vapor phase during thermal metamorphism or following a strong shock event (Krzysińska & Almeida, 2019; Wlotzka & Otto, 2012). If this vapor phase was hydrous, elevated water contents in olivine and orthopyroxene might be present.

Tuxtuac (LL5; fall October 1975; Figure S6B) also displays macroporosity and euhedral silicate crystals similar to Baszkówka albeit at much lower abundance (Graham et al., 1988; Matsumoto et al., 2016). We included these LL chondrites to test whether these lithologies contain detectable water in their silicates that would point to an oxidized, H₂O-rich metamorphic fluid as opposed to a reduced H₂- or CH₄-bearing fluid (Harries & Langenhorst, 2018).

Bensour (LL6; fall February 2002; Figure S6C) and Kheneg Ljouâd (LL5/6; fall July 2017; Figure S6D) are highly metamorphosed LL-type chondrites (Chennaoui & Garvie, 2018; Gattacceca et al., 2003) that closely resemble the material sampled on asteroid 25143 Itokawa by the Hayabusa mission (Nakamura et al., 2011) and possibly recorded the fluid activity in the LL parent body during thermal metamorphism.

Achondrites and NWA 7317: Zakødzie (Figure S7A) is an ungrouped enstatite achondrite which most likely represents an impact-melt breccia of enstatite chondritic parentage (Keil, 2010). Its mineralogy is highly reduced with nearly Fe-free orthopyroxene and clinopyroxene and graphite (Przylibski et al., 2005).

Dhofar 125 (Figure S7B) is an acapulcoite with low-Fe olivine (Fa_{8.5}) and orthopyroxene (Fs_{7.7}Wo_{1.9}; Grossman & Zipfel, 2001). As other samples of the acapulcoite-lodranite clan, it is the result of <20% partial

melting of a relatively reduced chondritic parent lithology and a low degree of melt migration (Floss, 2000; McCoy et al., 2019; Patzer et al., 2004). Dhofar 125 represents strongly heated, but essentially unfractionated, reduced material from the water-poor NC-type reservoir of the inner Solar System, which should not contain structurally bound water.

NWA 5480 (Figure S7C) is an olivine-rich, harzburgitic diogenite (Fa_{30.2}, Fs_{24.8}; Weisberg et al., 2009), which has undergone solid-state plastic deformation within its parent body 4 Vesta (Tkalcic & Brenker, 2015; Tkalcic et al., 2013).

NWA 4969 (Figure S7D) is an olivine-rich brachinite (Fa_{34.7}; Connolly et al., 2007), which represents an ultramafic residue from a low degree of partial melting in a presumably much smaller parent body (<100 km; Keil, 2014). Both samples represent the mantles of differentiated and relatively oxidized planetesimals of the NC-type reservoir, which could have preserved minor water contents of the initially accreted materials.

NWA 6693 (Figure S7E) is a FeO-rich achondrite of orthopyroxenitic composition (Fa_{49–53}, Fs_{42–43}Wo_{2.8–3.6}) and originated as an igneous cumulate or rapidly crystallized ultrabasic melt of a highly oxidized parent body (Garvie, 2012; Hibiya et al., 2019; Warren et al., 2013). NWA 6693 and its pairing NWA 6704 belong to a group of isotopically similar meteorites with strong affinities in $\Delta^{17}\text{O}$, $\epsilon^{54}\text{Cr}$, and $\epsilon^{50}\text{Ti}$ to CCs, indicating that melting and differentiation processes were also widespread in the CC-type reservoir of the protoplanetary disc (Sanborn et al., 2019). They stand out in containing abundant trails of μm -sized bubbles and bubble-bearing melt inclusions pointing to the presence of a volatile phase during crystallization. The bubbles do not show volatile species detectable by Raman micro-spectroscopy (Hibiya et al., 2019) but suggest that traces of water might have been present in the oxidized, FeO-rich parental melt.

NWA 7317 (Figure S7F) has been classified as a CR6 chondrite that contains relict chondrules in a strongly recrystallized groundmass (Fa_{38.0–38.2}, Fs_{29.3–29.4}Wo_{3.3–3.0}; Ruzicka et al., 2015). Together with NWA 6693/6704, it shares similar isotopic compositions with CR2 chondrites (Sanborn et al., 2019). However, Gardner-Vandy et al. (2012) and Agee et al. (2020) caution to link these meteorites to the CR2 parent body due to unresolved petrological mismatches, particularly in the Fe/Mg and Fe/Mn ratios. If indeed NWA 7317 originated from metamorphism of a hydrous CR2 protolith, elevated water contents in olivine and orthopyroxene might be expected.

Baszkówka, Bensour, and Kheneg Ljouâd are recent falls and the actual specimens studied show low degrees of weathering corresponding to grade W0 on the weathering scale of Wlotzka (1993). Our specimen of Tuxtuac shows slight limonitic staining by iron

oxyhydroxides surrounding metal inclusions. Limonitic staining and small limonitic veins are also observed in Zakødzic (Figure S7A). In our sample of Dhofar 125, pervasive limonitic veining occurs (Figure S7B) due to the extensive weathering of its content of metallic phases. Our sample of NWA 4969 is minimally weathered and shows only a moderate brownish staining with thin limonitic veins (Figure S7D). The other achondrites studied and NWA 7317 are very fresh, and our samples show no or only minimal evidence for limonitic staining or other weathering phenomena.

Sample Preparation

The reference olivine and orthopyroxene single crystals used for FT-IR spectroscopy were cut with a diamond wire saw perpendicular to the principal crystallographic directions (orthorhombic *a*, *b*, and *c* axes) based on external crystal morphology. In the case of the Jepara olivine, a simple slab was cut due to the absence of external morphology. Meteorite samples and remaining parts of the reference materials intended for NanoSIMS were cut into small slabs using the diamond wire saw and water as a cooling medium. The samples were immediately dried on a hot plate (110°C, ~60 s) and in a vacuum desiccator (room temperature).

We used glycol phthalate (Crystal Bond) to fix the reference and meteorite samples to the parallel polishing mount of a tripod polisher (South Bay Technology). Grinding and polishing were done manually on 800 grit SiC paper and finalized with 3- μm diamond using water and ethanol-based diamond suspension (Struers DP-Spray P). The final, cuboid-shaped single crystal reference samples for FT-IR spectroscopy were polished on all six sides except for the Jepara olivine slab, which was polished on two opposing sides. The reference and meteorite samples for NanoSIMS mounting were polished on two sides. After polishing, the samples were repeatedly leached with acetone to remove the glycol phthalate. They were finally cleaned in methanol and high-purity petroleum spirit with low evaporation residuals and water contents (<5 ppm, <0.5 ng L⁻¹).

The final state of the oriented single crystals for FT-IR spectroscopy was polished rectangular cuboids with edge lengths between 1.1 and 3.9 mm. Their precise dimensions were measured with a Mitutoyo digital micrometer providing an accuracy of $\pm 2 \mu\text{m}$. The final reference and meteorite samples for NanoSIMS mounting were double-polished slabs of 1–2 mm size and 0.5–1 mm thickness.

The reference and meteorite samples for NanoSIMS analysis were pressed into indium held in the innermost region (12 mm diameter) of two 25-mm aluminum sample disks. Each of the two mounts contained co-mounted

meteorite samples and all orthopyroxene and olivine reference samples, except for Jepara olivine being only available on one of the mounts. After pressing, the samples were level with the indium surface and the sample disk. The mounted samples were cleaned for approximately 20 min by low-angle Ar sputtering using a Leica RES102 ion mill (operated at 4° tilt, 8 kV, 4 mA). This step served to remove residues from solvents and surface layers containing crystallographic defects from polishing (e.g., Mamtani et al., 2020). These defects might accumulate hydroxyl groups during processing. Although the extent of this effect is not known, the ion polishing was added as a precautionary measure. The samples were imaged in a low-vacuum SEM at 20 keV without carbon coating and the mounts remained in high-vacuum until shipping to the OU NanoSIMS facility. Prior to loading into the NanoSIMS, the samples were sputter-coated with gold.

FT-IR Spectroscopy

FT-IR spectroscopy was conducted at the Department of Mineralogy of the Geoscience Center Göttingen and used a Bruker Vertex 70 spectrometer with a Hyperion 3000 infrared microscope equipped with Cassegrain optics, a KBr beamsplitter, a liquid nitrogen-cooled D316-025 mercury cadmium telluride detector, a SiC global light source, and a ZnSe wire grid polarizer. The samples were placed on a CaF₂ support plate or positioned onto apertures drilled into a thin brass plate. Spectra were recorded under ambient conditions in the wavenumber range of 600–6000 cm⁻¹ with a resolution of 2 cm⁻¹ by accumulating 32–128 scans on blank reference and sample. The field of view was adjusted between 30 × 30 and 100 × 100 μm^2 . Spectrometer and microscope were purged with dry air to minimize the signals of atmospheric H₂O and CO₂.

For each single crystal of the olivine and orthopyroxene reference samples, absorption spectra were obtained with the beam direction parallel to the principal crystallographic axes, which were parallel to the cuboids' edges (Figures S1–S5). During this procedure, two spectra of perpendicular polarization directions were acquired for each of the three beam directions, such that each of the principal absorption spectra was obtained twice at different thickness. Thickness-normalized spectral absorbances near the hydroxyl stretching region were baseline corrected in the wavenumber range of 2200–4300 cm⁻¹ using asymmetric least squares (ALS) in the R package *baseline* (Liland et al., 2010). The ALS parameter λ was set between 4.0 and 5.0 and the weighting of positive residuals was set to 0.001.

For olivine, the thickness-normalized spectral absorbances were integrated in the region of 3350–3750

cm^{-1} to obtain integrated absorbances along the principal directions. The two values obtained for each of the principal direction at different thickness typically deviated <14% and in most cases <4%. These two values were averaged and the three averages representing the principal integrated absorbances were summed to obtain the total integrated absorbance. H_2O contents in parts per million by mass (ppmw) were calculated from the total integrated absorbances using an integral specific absorption coefficient of $0.188 \text{ cm}^2 \text{ ppmw H}_2\text{O}$ of Bell et al. (2003).

For orthopyroxene, the thickness-normalized spectral absorbances were integrated in the region of $2800\text{--}3650 \text{ cm}^{-1}$ in four sections separated at 3200 , 3475 , and 3550 cm^{-1} and corresponding to specific absorption bands. For each integrated section, a frequency-dependent extinction coefficient was calculated via the calibrations of Stalder et al. (2012), assuming band centers to be at 3070 cm^{-1} (A_4), 3420 cm^{-1} (A_3), 3520 cm^{-1} (A_2), and 3600 cm^{-1} (A_1). The partial H_2O contents corresponding to each band were then summed for each principal spectrum. The deviations of the values obtained for the two equivalent spectra taken at different thickness were typically <4% with the exception of the weakest absorption directions, where deviations of 9% and 21% occurred in two separate samples of the same Kilosa enstatite crystal. The averaged partial H_2O contents of the three principal directions were finally summed to obtain the total H_2O content.

NanoSIMS Analysis

SIMS analysis used the CAMECA NanoSIMS 50 L at Open University, Milton Keynes (UK). The instrument was operated with a Cs^+ primary beam using a current of 1 nA at 16 keV ion energy. The beam was first rastered over $15 \times 15 \mu\text{m}$ for 2 min prior to analyses to remove the gold coating and possible surface contaminations. The rastered area was reduced to $10 \times 10 \mu\text{m}$ for analyses and only secondary ions from the central $5 \times 5 \mu\text{m}$ (25%) were extracted by beam blanking. The instrument was set up with a mass resolving power of ~4000 (CAMECA definition—see Hoppe et al., 2013) and the masses recorded were ^1H , ^2H , and ^{13}C on electron multipliers, and ^{16}O on a Faraday cup. Each measurement consisted of 200 cycles, with a total measurement time of 2 min. The total ^{16}O counts for typical analysis were around 1×10^{10} . Charge compensation was provided by the electron flood gun. The vacuum pressure in the analysis chamber was typically 5×10^{-10} mbar.

Surface contamination of our samples by hydrocarbons was evaluated using the $^{13}\text{C}/^{16}\text{O}$ ion ratio during and after the analysis. Some analysis spots were flagged during acquisition as contamination became

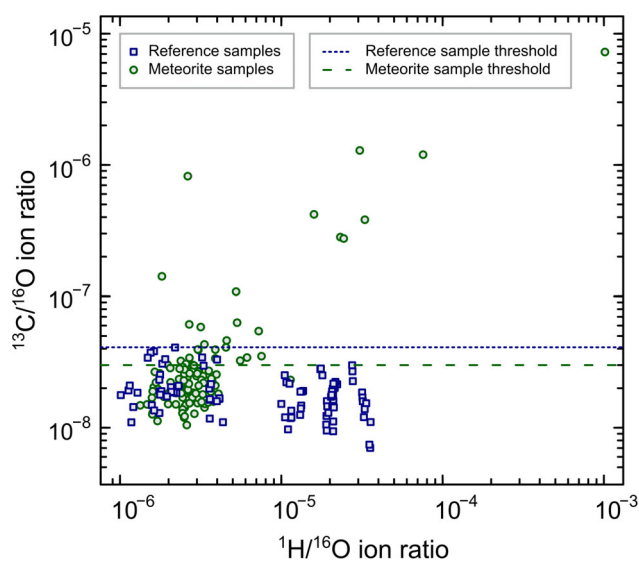


FIGURE 1. NanoSIMS carbon contamination monitoring. Measurements with $^{13}\text{C}/^{16}\text{O}$ ion ratios above the thresholds were dismissed. The threshold for measurements on reference samples (4.1×10^{-8}) was chosen less strict than the threshold for meteorite samples (3×10^{-8}), because some blanks occasionally showed slightly elevated $^{13}\text{C}/^{16}\text{O}$ ratios, although their $^1\text{H}/^{16}\text{O}$ ion ratios remained at the lowest measured. Samples in-between the two thresholds are marked as suspect, while those above were fully excluded. The two measurements with $^1\text{H}/^{16}\text{O} < 3 \times 10^{-6}$ and $^{13}\text{C}/^{16}\text{O} > 10^{-7}$ might indicate elevated indigenous carbon or hydrogen-poor carbon contamination. (Color figure can be viewed at wileyonlinelibrary.com.)

evident. During post-processing, we used a $^{13}\text{C}/^{16}\text{O}$ threshold of 3×10^{-8} , above which we flagged sample analyses for quantification due to suspected contamination, evident as a correlation of $^1\text{H}/^{16}\text{O}$ and $^{13}\text{C}/^{16}\text{O}$ ion ratios (Figure 1). We derived the threshold value as the upper limit of the $^{13}\text{C}/^{16}\text{O}$ ratios obtained from the analysis of our terrestrial reference samples, which we deem nearly free of hydrocarbon contamination, because they are non-porous and intensively cleaned single crystal samples. For calibration, we accepted $^{13}\text{C}/^{16}\text{O}$ ion ratios up to 4.1×10^{-8} , because Jepara olivine and Neuschwanstein enstatite used as blanks occasionally showed slightly elevated values, although the $^1\text{H}/^{16}\text{O}$ ion ratios remained at the lowest measured. Cutting them off would have removed valuable $^1\text{H}/^{16}\text{O}$ reference measurements. This suggests that carbon contamination or indigenous carbon was not necessarily hydrogen bearing. Such carbon might be due to contamination during SEM imaging or truly indigenous carbon in the mineral structure. In the case of Neuschwanstein, graphite occurs in the sample and indicates high indigenous carbon activity. In the final quantification, any sample with $^{13}\text{C}/^{16}\text{O} > 4.1 \times 10^{-8}$ was excluded, while those few in-between 3×10^{-8} and 4.1×10^{-8} are marked in our results.

TABLE 2. FT-IR results of Ol24345-1-1 (Mogok olivine).

Orientation	Variant ^a	Thickness (cm)	Absorbance (cm ⁻²)	H ₂ O (ppmw)
E [100]	SM	0.2054	18.8	3.5
E [100]	LM	0.2752	21.2	4.0
	Average		20.0	3.8
E [010]	SL	0.2054	7.8	1.5
E [010]	ML	0.2495	7.8	1.5
	Average		7.8	1.5
E [001]	MS	0.2495	5.2	1.0
E [001]	LS	0.2752	5.0	0.9
	Average		5.1	1.0
	Sum of averages		32.9	6.2

Abbreviations: FT-IR, Fourier transform infrared; L, largest edge; M, intermediate edge; S, smallest edge; for example, SM = IR beam parallel to shortest edge and polarization E vector parallel to intermediate edge.

^aEdge lengths of the rectangular cuboids.

TABLE 3. FT-IR results of Ol2536-1-1 (Sapat olivine).

Orientation	Variant ^a	Thickness (cm)	Absorbance (cm ⁻²)	H ₂ O (ppmw)
E [100]	MS	0.1252	157.0	29.5
E [100]	LS	0.2171	154.2	29.0
	Average		155.6	29.3
E [010]	SM	0.1131	224.6	42.2
E [010]	LM	0.2171	222.8	41.9
	Average		223.7	42.1
E [001]	SL	0.1131	48.0	9.0
E [001]	ML	0.1252	47.4	8.9
	Average		47.7	9.0
	Sum of averages		427.0	80.3

Abbreviation: FT-IR, Fourier transform infrared.

^aSee Table 2.

FT-IR-NanoSIMS Calibration Procedure

The results from FT-IR spectroscopic analysis of the reference samples are given in Tables 2–5. Our samples of Mogok and Sapat olivine resulted in 6.2 ppmw H₂O and 80.3 ppmw H₂O, respectively. Our two samples of the same Kilosa orthopyroxene crystal resulted in 32.8 and 32.9 ppmw H₂O. Our sample of Mogok orthopyroxene resulted in 64.8 ppmw H₂O. The uncertainty of the H₂O contents due to the data reduction procedure mainly stems from the baseline subtraction, which we tested by varying the ALS λ parameter to ± 0.5 about its chosen value. This resulted in variations of the final H₂O contents of less than $\pm 10\%$ to about $\pm 20\%$ relative to the value obtained with the adopted λ (largest variation in the case of Mogok orthopyroxene displaying a set of closely overlapping absorption bands). This range approximately represents a two-standard-deviation uncertainty due to the somewhat arbitrary choice of the ALS λ baseline parameter.

Jepara olivine did not show any OH absorption bands at a thickness of 2.3 mm when measured in two random but perpendicular polarization directions at a field of view of approximately $30 \times 30 \mu\text{m}^2$. We treated this spectrum analogously to the terrestrial olivines using the calibration of Bell et al. (2003) and estimate a thickness-dependent detection limit of 0.028 cm ppmw H₂O from the 3SD statistical variations of the integrated background (the detection limit calculates as this value divided by the actual thickness). At 2.3 mm thickness, the detection limit corresponds to 0.12 ppmw partial H₂O in a given polarization direction or 0.36 ppmw total H₂O for the sum of three independent directions. Based on these considerations, we adopted our Jepara olivine sample as a blank reference to characterize background hydrogen during our NanoSIMS measurements.

For orthopyroxene analyses, we were not able to source a sufficiently large blank sample for FT-IR spectroscopy and, instead, assumed that the enstatite of the Neuschwanstein EL6 chondrite represents the blank reasonably well, because it resulted in very low ¹H/¹⁶O ion ratios that are comparable with those of Jepara olivine, averaging $(0.16 \pm 0.04) \times 10^{-5}$ ($n = 6$) and $(0.17 \pm 0.01) \times 10^{-5}$ ($n = 9$), respectively. The ¹H/¹⁶O ion ratios measured on Neuschwanstein and Jepara are consistently the lowest of all our samples. Because our second indium mount did not contain Jepara olivine or Neuschwanstein enstatite, we used San Carlos olivine on an OU mount as a another low-concentration reference for olivine and orthopyroxene. Previous measurements of this San Carlos olivine calibrated with Mogok, Sapat, and Jepara olivine resulted in a mean H₂O content of 2.8 ± 2.1 ppmw. We adopted this as the working reference value at quasi-blank concentration, as it is close to the detection limit.

The linear regressions of the measured ion ratios of the reference samples against the known H₂O contents provide relative sensitivity factors (slopes), blank offsets (intercepts), and envelopes of the confidence and prediction intervals. The confidence envelope at a given level (e.g., 95.5%) provides the confidence interval for the mean ¹H/¹⁶O ratio at a given H₂O content, that is, for the central fit line. It is comparable to the standard error of the mean and describes the fit based on the whole of the data points. The prediction envelope provides the prediction interval for single data points of the ¹H/¹⁶O ratio at a given H₂O content and confidence level. It is comparable to a scaled standard deviation (SD) giving the range about a central mean value where single datapoints can be expected to occur with a given confidence. Having this information at hand, we calculate the detection limit not from the SD of the blank alone, but from the prediction interval at zero H₂O content (Figure 2). In this way, the detection limit not only relies on the statistical variation of the blank measurements (for which only few measurements are

TABLE 4. FT-IR results of En24345-1-1 (Mogok orthopyroxene).

Orientation	Variant ^a	Thickness (cm)	Absorbances of bands A ₁ to A ₄				H ₂ O (ppmw)
			A ₁ (cm ⁻²)	A ₂ (cm ⁻²)	A ₃ (cm ⁻²)	A ₄ (cm ⁻²)	
E [100]	SM	0.1790	19.0	44.1	156.9	2.9	28.6
E [100]	LM	0.3189	17.9	43.2	162.9	2.0	28.7
	Average		18.5	43.7	159.9	2.5	28.7
E [010]	SL	0.1790	20.4	26.9	49.6	33.5	16.4
E [010]	ML	0.2185	19.7	25.3	46.7	39.6	15.9
	Average		20.1	26.1	48.2	36.6	16.2
E [001]	MS	0.2185	14.9	39	91.0	8.7	19.8
E [001]	LS	0.3189	14.8	39.6	91.4	8.7	20.1
	Average		14.9	39.3	91.2	8.7	20.0
	Sum of averages		53.4	109.1	299.3	47.7	64.8

Abbreviation: FT-IR, Fourier transform infrared.

^aSee Table 1.

TABLE 5. FT-IR results of En206269-1-1 and En206269-1-2 (Kilosa orthopyroxene, two subsamples).

Orientation	Variant ^a	Thickness (cm)	Absorbances of bands A ₁ to A ₄				H ₂ O (ppmw)
			A ₁ (cm ⁻²)	A ₂ (cm ⁻²)	A ₃ (cm ⁻²)	A ₄ (cm ⁻²)	
<i>En206269-1-1</i>							
E [100]	SM	0.1064	4.6	10.3	20.5	9.0	5.4
E [100]	LM	0.3625	4.1	9.9	17.6	12.0	5.1
	Average		4.4	10.1	19.1	10.5	5.3
E [010]	MS	0.2841	3.4	15.8	9.4	68.1	7.7
E [010]	LS	0.3625	2.9	15.7	9.0	68.0	7.5
	Average		3.2	15.8	9.2	68.1	7.6
E [001]	SL	0.1064	10.2	75.9	29.5	49.7	20.1
E [001]	ML	0.2841	10.0	73.3	28.7	52.6	19.7
	Average		10.1	74.6	29.1	51.2	19.9
	Sum of averages		17.6	100.5	57.4	129.7	32.8
<i>En206269-1-2</i>							
E [100]	SL	0.2137	4.0	9.5	18.8	11.5	5.1
E [100]	ML	0.3622	3.0	8.0	16.5	8.0	4.2
	Average		3.5	8.8	17.7	9.8	4.7
E [010]	MS	0.3622	2.9	17.1	9.1	68.8	7.8
E [010]	LS	0.3946	2.5	15.4	8.6	69.2	7.4
	Average		2.7	16.3	8.9	69.0	7.6
E [001]	SM	0.2137	10.5	77.2	29.8	53.8	20.6
E [001]	LM	0.3946	10.3	77.0	31.2	53.9	20.7
	Average		10.4	77.1	30.5	53.9	20.7
	Sum of averages		16.6	102.1	57.0	132.6	32.9

Abbreviation: FT-IR, Fourier transform infrared.

^aSee Table 1.

available) but on the whole calibration, incorporating the overall quality of the fit and a much larger number of reference data points. Hence, a poor calibration will result in a poor detection limit in terms of ppmw H₂O, which, therefore, is stricter than a detection limit solely based on blank measurements.

The NanoSIMS analyses were conducted on five consecutive days, for each of which we obtained mineral-specific calibrations for either olivine or orthopyroxene after daily tuning of the instrument (Figure 3, Table 6),

except on the first day when calibration for both olivine and orthopyroxene was obtained. The daily calibration curves were obtained by linearly regressing the adopted H₂O contents of the reference samples against the measured ¹H/¹⁶O ion ratios, which we measured at least three to six times on the reference and blank samples (Tables S1 and S2). Sets of reference measurements conducted early and late in the sessions showed no significant differences of the mean ¹H/¹⁶O ion ratios, indicating negligible drift during the day.

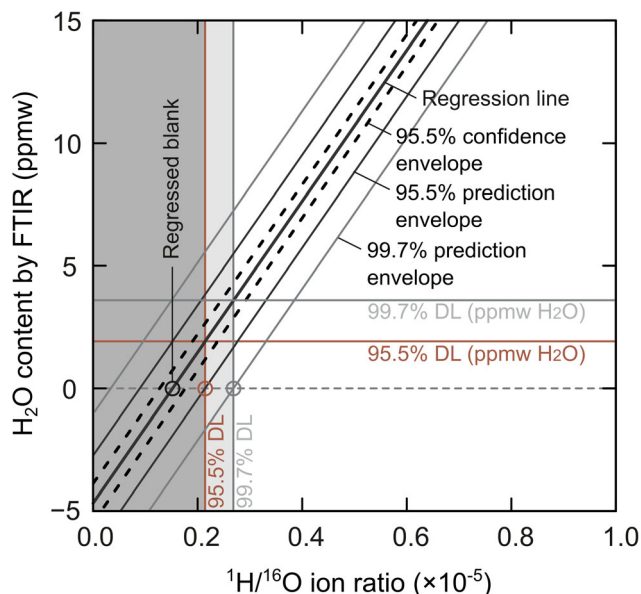


FIGURE 2. Principle of the determination of detection limits (DL) using a regressed blank. The regression line through the data points (not shown) intersects zero H_2O content at the regressed blank. Based on the residuals of the fit, confidence and prediction intervals and envelopes can be calculated for given probabilities, here 95.5% and 99.7% (99.7% confidence envelope not shown). The intersection of the upper prediction envelope with zero H_2O content defines the detection limit in terms of the ion ratio at the given probability. (Color figure can be viewed at wileyonlinelibrary.com.)

The procedure helps to provide a useful detection limit when a true blank is not available, as in case of our San Carlos olivine with barely detectable H_2O . Moreover, it requires only a relatively small number of measurements at blank or near-blank levels, whereas solely obtaining the detection limit from the SD of the blank measurements requires a large number of such measurements to provide statistical robustness. This would require a large overhead of time on the instrument just to conduct blank measurements. On the downside, the regressed detection limits are susceptible to systematic errors of the calibrated reference values of the standards used.

We derived detection limits at confidence levels of 95.5% (about two SDs) and 99.7% (about three SDs) in terms of the $^1\text{H}/^{16}\text{O}$ ratios and converted these into H_2O contents using the respective linear calibrations (Table 6). For olivine at 95.5% confidence, we obtain detection limits of 1.9, 2.1, and 3.3 ppmw H_2O in sessions 1, 2, and 5, respectively. At 99.7% confidence, the detection limits are 3.6, 3.6, and 5.4 ppmw H_2O , respectively. For orthopyroxene at 95.5% confidence, we obtain detection limits of 5.9, 4.6, and 6.9 ppmw H_2O in sessions 1, 3, and 4, respectively. At 99.7% confidence, the detection limits are 10.8, 7.7, and 10.9 ppmw H_2O , respectively. The higher detection limits of the

orthopyroxene mainly stem from the larger scatter of the FT-IR-derived reference values of the standards.

Robustness of the FT-IR-NanoSIMS Calibration

The integral specific absorption coefficient of $0.188 \text{ cm}^2 \text{ ppmw H}_2\text{O}$ adopted from Bell et al. (2003) to calculate H_2O contents in olivine from FT-IR absorbances is larger than the value of $0.119 \text{ cm}^2 \text{ ppmw H}_2\text{O}$ published by Withers et al. (2012). Accordingly, the H_2O contents of our reference olivines are about 60% larger than the values that can be derived using the latter calibration. For orthopyroxene, the frequency-dependent calibration of Stalder et al. (2012) used here results in H_2O contents that are larger by about 60% (Kilosa orthopyroxene) and 90% (Mogok orthopyroxene) relative to the calibration of Bell et al. (1995), which uses a simple, fixed absorption coefficient. We chose this approach of calculating H_2O contents (“Bell03-Stalder”), because the use of the coefficients is established and has been studied extensively.

Notably, the Bell03-Stalder FT-IR calibrations potentially overestimate H_2O contents relative to the combination of Withers et al. (2012) for olivine and Bell et al. (1995) for orthopyroxene (“Withers-Bell95”). In turn, the resulting NanoSIMS detection limits for Bell03-Stalder are larger and, therefore, somewhat more pessimistic. We use this to provide reasonable upper limits of the H_2O contents of the NAMs analyzed by NanoSIMS without minimizing detection limits via choosing an apparently more favorable FT-IR calibration and relying too much on its external accuracy. Choosing Withers-Bell95 as an alternative calibration set for olivine and orthopyroxene reduces the 99.7% detection limits to ~ 4 ppmw H_2O for olivine and to ~ 5 ppmw H_2O for orthopyroxene. It should be noted that the uncertainty in detection limits dominantly stems from the external calibration of the reference materials and not from the internal reproducibility of the NanoSIMS analyses. Hence, better characterized reference materials could considerably improve trace-level H_2O determinations.

RESULTS

None of the samples analyzed by NanoSIMS consistently shows H_2O contents in olivine or orthopyroxene above the detection limits at a 99.7% level of confidence (Tables 7 and 8, Figure 4). In any case, their H_2O contents are lower than 10.9 ppmw, the largest detection limit at this level of confidence using the Bell-Stalder calibration. (Using the Withers-Bell95 calibration, the quantified H_2O contents of orthopyroxene shift to lower values and the relative distances to the detection limits become lower, but only few analyses barely exceed the 99.7% detection limits. None of the contamination-

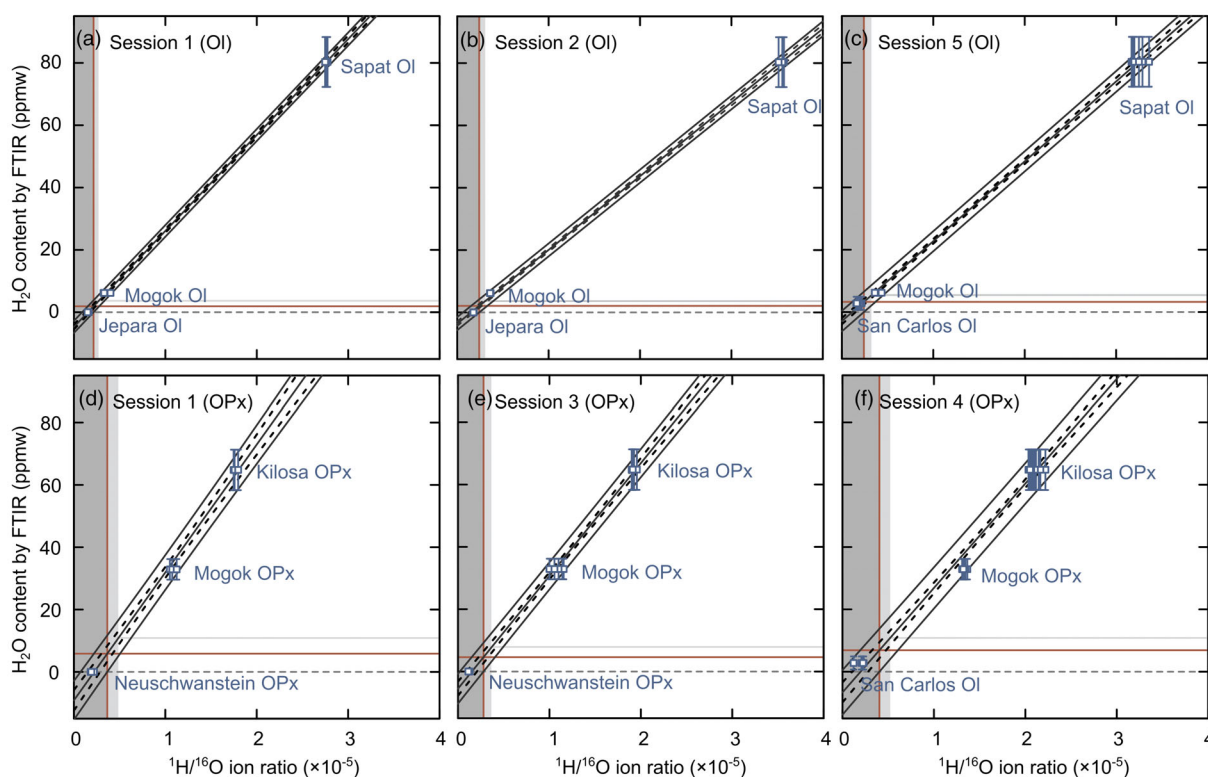


FIGURE 3. NanoSIMS calibration data. The outline of the plots follows Figure 2 (99.7% prediction envelope not shown). The vertical error bars correspond to 10% relative uncertainty of the FT-IR H₂O contents. (a–c) Sessions 1, 2, and 5 for olivine (Ol). (d–f) Sessions 1, 3, and 4 for orthopyroxene (OPx). In session 4, San Carlos olivine was used as near-blank reference due to the lack of a suitable orthopyroxene on the sample mount used in this session. (Color figure can be viewed at wileyonlinelibrary.com.)

TABLE 6. Parameters of the NanoSIMS calibration.

Mineral	Session	Intercept		Regressed blank ion ratio, ¹ H/ ¹⁶ O	DL95 (95.5%)		DL99 (99.7%)	
		(ppmw), H ₂ O	Slope (ppmw) H ₂ O		¹ H/ ¹⁶ O	ppmw, H ₂ O	¹ H/ ¹⁶ O	ppmw, H ₂ O
Ol	1	-4.7 ± 0.3	(3.08 ± 0.02) × 10 ⁶	(1.5 ± 0.1) × 10 ⁻⁶	2.1 × 10 ⁻⁶	1.9	2.7 × 10 ⁻⁶	3.6
Ol	2	-3.6 ± 0.3	(2.37 ± 0.02) × 10 ⁶	(1.5 ± 0.1) × 10 ⁻⁶	2.4 × 10 ⁻⁶	2.1	3.1 × 10 ⁻⁶	3.6
Ol	5	-2.9 ± 0.5	(2.56 ± 0.02) × 10 ⁶	(1.1 ± 0.2) × 10 ⁻⁶	2.4 × 10 ⁻⁶	3.3	3.2 × 10 ⁻⁶	5.4
OPx	1	-9.1 ± 1.4	(4.10 ± 0.12) × 10 ⁶	(2.2 ± 0.3) × 10 ⁻⁶	3.6 × 10 ⁻⁶	5.9	4.9 × 10 ⁻⁶	10.8
OPx	3	-5.5 ± 1.1	(3.62 ± 0.08) × 10 ⁶	(1.5 ± 0.3) × 10 ⁻⁶	2.8 × 10 ⁻⁶	4.6	3.6 × 10 ⁻⁶	7.7
OPx	4	-6.6 ± 1.6	(3.35 ± 0.09) × 10 ⁶	(2.0 ± 0.4) × 10 ⁻⁶	4.0 × 10 ⁻⁶	6.9	5.2 × 10 ⁻⁶	10.9

free olivine analyses exceed the 99.7% detection limits. Below we only consider the Bell03-Stalder calibration.)

At a level of confidence of 95.5%, the olivine of Baszkówka shows H₂O contents that are barely but consistently above the detection limit of 2.1 ppmw H₂O, amounting to an average of 2.6 ± 2.1 ppmw H₂O. Similarly, olivine of Bensour (2 of 3), Dhofar 125 (6 of 7), NWA 4969 (12 of 12), and NWA 6693 (4 of 4) shows H₂O contents above the respective detection limits at 95.5% confidence, amounting to average contents of 3.9 ± 2.1 to 4.4 ± 3.3 ppmw H₂O. We caution that the uncertainty of these values is very large and that undetected sources of

contamination, such a carbon-poor hydrogen compounds and especially iron oxyhydroxides from porosity and fractures, might have contributed to the secondary ion signal. NWA 4969 and Dhofar 125 in particular are moderately to strongly stained by iron oxyhydroxide from the weathering of iron sulfide and metal components.

Only NWA 4969 and NWA 6693 have sufficiently large grain sizes and contain fracture-free crystals that allowed for the production of doubly polished slabs of reasonable quality and thickness (147 and 204 μm, respectively) for polarized FT-IR spectroscopy. None of the spectra obtained from random crystal orientations in

TABLE 7. NanoSIMS results of H₂O in olivine and orthopyroxene of ordinary chondrites.

Sample	Mineral	Session	¹³ C/ ¹⁶ O ion ratio	¹ H/ ¹⁶ O ion ratio ^a	Cal. H ₂ O (ppmw) ^a	Final H ₂ O (ppmw) ^b
Baszkówka	Ol	1	3.4 × 10 ⁻⁸	(0.390 ± 0.002) × 10 ⁻⁵	7.3 ± 1.9	(7.3 ± 1.9)
Baszkówka	Ol	1	3.4 × 10 ⁻⁸	(0.269 ± 0.002) × 10 ⁻⁵	3.6 ± 1.9	(3.6 ± 1.9)
Baszkówka	Ol	2	3.3 × 10 ⁻⁸	(0.556 ± 0.004) × 10 ⁻⁵	9.5 ± 2.1	(9.5 ± 2.1)
Baszkówka	Ol	2	2.1 × 10 ⁻⁸	(0.251 ± 0.058) × 10 ⁻⁵	2.3 ± 2.1	<3.6
Baszkówka	Ol	2	2.0 × 10 ⁻⁸	(0.247 ± 0.002) × 10 ⁻⁵	2.3 ± 2.1	<3.6
Baszkówka	Ol	2	1.5 × 10 ⁻⁸	(0.303 ± 0.002) × 10 ⁻⁵	3.6 ± 2.1	<3.6
Baszkówka	Ol	2	1.8 × 10 ⁻⁸	(0.263 ± 0.002) × 10 ⁻⁵	2.6 ± 2.1	<3.6
Baszkówka	Ol	2	1.7 × 10 ⁻⁸	(0.255 ± 0.002) × 10 ⁻⁵	2.4 ± 2.1	<3.6
Baszkówka	Ol	2	1.5 × 10 ⁻⁸	(0.253 ± 0.002) × 10 ⁻⁵	2.4 ± 2.1	<3.6
Baszkówka	OPx	1	1.8 × 10 ⁻⁸	(0.265 ± 0.002) × 10 ⁻⁵	1.7 ± 5.9	<5.9
Baszkówka	OPx	1	1.8 × 10 ⁻⁸	(0.223 ± 0.002) × 10 ⁻⁵	0.0 ± 6.0	<5.9
Baszkówka	OPx	1	2.7 × 10 ⁻⁸	(0.308 ± 0.002) × 10 ⁻⁵	3.5 ± 5.9	<5.9
Baszkówka	OPx	3	1.1 × 10 ⁻⁸	(0.171 ± 0.001) × 10 ⁻⁵	0.7 ± 4.7	<4.6
Baszkówka	OPx	3	1.5 × 10 ⁻⁸	(0.199 ± 0.001) × 10 ⁻⁵	1.7 ± 4.7	<4.6
Baszkówka	OPx	3	1.3 × 10 ⁻⁸	(0.159 ± 0.001) × 10 ⁻⁵	0.2 ± 4.7	<4.6
Baszkówka	OPx	3	1.7 × 10 ⁻⁸	(0.158 ± 0.001) × 10 ⁻⁵	0.2 ± 4.7	<4.6
Bensour	Ol	5	2.4 × 10 ⁻⁸	(0.368 ± 0.002) × 10 ⁻⁵	6.5 ± 3.2	6.5 ± 3.2
Bensour	Ol	5	2.6 × 10 ⁻⁸	(0.270 ± 0.002) × 10 ⁻⁵	4.0 ± 3.3	<5.4
Bensour	Ol	5	1.9 × 10 ⁻⁸	(0.207 ± 0.001) × 10 ⁻⁵	2.4 ± 3.3	<3.3
Bensour	OPx	4	1.7 × 10 ⁻⁸	(0.303 ± 0.002) × 10 ⁻⁵	3.5 ± 7.0	<6.9
Bensour	OPx	4	2.0 × 10 ⁻⁸	(0.260 ± 0.002) × 10 ⁻⁵	2.1 ± 7.0	<6.9
Bensour	OPx	4	1.9 × 10 ⁻⁸	(0.264 ± 0.002) × 10 ⁻⁵	2.2 ± 7.0	<6.9
Bensour	OPx	4	2.3 × 10 ⁻⁸	(0.320 ± 0.002) × 10 ⁻⁵	4.1 ± 6.9	<6.9
Kheneg Ljouâd	Ol	1	3.2 × 10 ⁻⁸	(0.238 ± 0.002) × 10 ⁻⁵	2.7 ± 1.9	(<3.6)
Kheneg Ljouâd	Ol	1	2.6 × 10 ⁻⁸	(0.176 ± 0.001) × 10 ⁻⁵	0.7 ± 1.9	<1.9
Kheneg Ljouâd	OPx	3	3.4 × 10 ⁻⁸	(0.613 ± 0.003) × 10 ⁻⁵	16.7 ± 4.5	(16.7 ± 4.5)
Kheneg Ljouâd	OPx	3	3.9 × 10 ⁻⁸	(0.390 ± 0.008) × 10 ⁻⁵	8.6 ± 4.6	(8.6 ± 4.6)
Kheneg Ljouâd	OPx	3	2.9 × 10 ⁻⁸	(0.205 ± 0.001) × 10 ⁻⁵	1.9 ± 4.7	<4.6
Kheneg Ljouâd	OPx	3	2.2 × 10 ⁻⁸	(0.206 ± 0.001) × 10 ⁻⁵	2.0 ± 4.7	<4.6
Tuxtuac	Ol	2	3.1 × 10 ⁻⁸	(0.256 ± 0.002) × 10 ⁻⁵	2.5 ± 2.1	(<3.6)
Tuxtuac	Ol	2	1.4 × 10 ⁻⁸	(0.252 ± 0.002) × 10 ⁻⁵	2.4 ± 2.1	<3.6
Tuxtuac	Ol	2	1.8 × 10 ⁻⁸	(0.202 ± 0.002) × 10 ⁻⁵	1.2 ± 2.1	<2.1
Tuxtuac	OPx	3	3.0 × 10 ⁻⁸	(0.284 ± 0.002) × 10 ⁻⁵	4.8 ± 4.6	(<7.7)
Tuxtuac	OPx	3	1.9 × 10 ⁻⁸	(0.160 ± 0.001) × 10 ⁻⁵	0.3 ± 4.7	<4.6
Tuxtuac	OPx	3	1.5 × 10 ⁻⁸	(0.133 ± 0.001) × 10 ⁻⁵	-0.7 ± 4.7	<4.6

^a95.5% confidence intervals.

^bFinal H₂O is the calculated H₂O content screened for the detection limits at 99.7% and 95.5% confidence, either stating the value (if above the 99.7% limit), the 99.7% upper limit (if above the 95.5% limit) or the 95.5% upper limit (if below). Values in bracket are those that have ¹³C/¹⁶O > 3 × 10⁻⁸ and are suspect of hydrocarbon contamination.

these samples shows discernable OH absorption features. Applying the detection limit of 0.028 cm ppmw H₂O for olivine, this corresponds to upper limits of about 1.9–1.4 ppmw partial H₂O, respectively. Unless we serendipitously encountered polarization directions with low absorbance only, it seems very unlikely that olivine and orthopyroxene of NWA 4969 and NWA 6693 contain H₂O greater than 2 ppmw.

DISCUSSION

H₂O Solubility in Asteroid Interiors

Exemplarily, we treat the solubility of H₂O in orthopyroxene of the LL parent body to illustrate the

behavior of H₂O under metamorphic conditions. Harries and Langenhorst (2018) inferred that the initial ice/rock ratio was about 7 × 10⁻³ by mass (or about 700 ppmw bulk H₂O) at the origin of their sample within the LL parent body. In principle, this leaves some room for the dissolution of H₂O into NAMs at higher metamorphic grade, but the solubility sensitively depends on temperature, pressure, H₂O fugacity, and co-substituting cations.

According to Mierdel and Keppler (2004), the H₂O content of enstatite follows the relation $W_{\text{H}_2\text{O}} = Af_{\text{H}_2\text{O}} \exp(-\Delta H/RT) \exp(-P\Delta V/RT)$, where $A = 0.01354$ ppmw ($f_{\text{H}_2\text{O}}$ relative to 1 bar H₂O), $\Delta H = -4563$ J mol⁻¹, and $\Delta V = 12.1$ cm³ mol⁻¹. Pressure is one of the most crucial parameters and least constrained with respect to the metamorphic equilibration of ordinary

TABLE 8. NanoSIMS results of H₂O in olivine and orthopyroxene of achondrites and NWA 7317.

Sample	Mineral	Session	¹³ C/ ¹⁶ O ion ratio	¹ H/ ¹⁶ O ion ratio ^a	Cal. H ₂ O (ppmw) ^a	Final H ₂ O (ppmw) ^b
Zakøodzie	OPx	4	1.8 × 10 ⁻⁸	(0.284 ± 0.002) × 10 ⁻⁵	2.9 ± 7.0	<6.9
Zakøodzie	OPx	4	2.1 × 10 ⁻⁸	(0.390 ± 0.002) × 10 ⁻⁵	6.4 ± 6.9	<6.9
Zakøodzie	OPx	4	2.5 × 10 ⁻⁸	(0.327 ± 0.002) × 10 ⁻⁵	4.3 ± 6.9	<6.9
Zakøodzie	OPx	4	1.8 × 10 ⁻⁸	(0.407 ± 0.002) × 10 ⁻⁵	7.0 ± 6.9	<10.9
Dhofar 125	Ol	2	2.2 × 10 ⁻⁸	(0.252 ± 0.002) × 10 ⁻⁵	2.4 ± 2.1	<3.6
Dhofar 125	Ol	2	2.0 × 10 ⁻⁸	(0.162 ± 0.002) × 10 ⁻⁵	0.2 ± 2.1	<2.1
Dhofar 125	Ol	2	2.4 × 10 ⁻⁸	(0.262 ± 0.002) × 10 ⁻⁵	2.6 ± 2.1	<3.6
Dhofar 125	Ol	5	1.6 × 10 ⁻⁸	(0.379 ± 0.002) × 10 ⁻⁵	6.8 ± 3.2	6.8 ± 3.2
Dhofar 125	Ol	5	1.4 × 10 ⁻⁸	(0.334 ± 0.002) × 10 ⁻⁵	5.7 ± 3.2	5.7 ± 3.2
Dhofar 125	Ol	5	1.5 × 10 ⁻⁸	(0.336 ± 0.002) × 10 ⁻⁵	5.7 ± 3.2	5.7 ± 3.2
Dhofar 125	Ol	5	1.0 × 10 ⁻⁸	(0.259 ± 0.002) × 10 ⁻⁵	3.7 ± 3.3	<5.4
Dhofar 125	OPx	4	2.5 × 10 ⁻⁸	(0.396 ± 0.002) × 10 ⁻⁵	6.7 ± 6.9	<6.9
Dhofar 125	OPx	4	2.3 × 10 ⁻⁸	(0.373 ± 0.002) × 10 ⁻⁵	5.9 ± 6.9	<6.9
Dhofar 125	OPx	4	1.9 × 10 ⁻⁸	(0.366 ± 0.002) × 10 ⁻⁵	5.6 ± 6.9	<6.9
NWA 5480	OPx	4	2.5 × 10 ⁻⁸	(0.298 ± 0.002) × 10 ⁻⁵	3.4 ± 7.0	<6.9
NWA 5480	OPx	4	2.6 × 10 ⁻⁸	(0.301 ± 0.002) × 10 ⁻⁵	3.5 ± 7.0	<6.9
NWA 5480	OPx	4	2.0 × 10 ⁻⁸	(0.259 ± 0.001) × 10 ⁻⁵	2.1 ± 7.0	<6.9
NWA 4969	Ol	5	1.7 × 10 ⁻⁸	(0.281 ± 0.001) × 10 ⁻⁵	4.3 ± 3.3	<5.4
NWA 4969	Ol	5	1.5 × 10 ⁻⁸	(0.256 ± 0.001) × 10 ⁻⁵	3.6 ± 3.3	<5.4
NWA 4969	Ol	5	1.5 × 10 ⁻⁸	(0.270 ± 0.001) × 10 ⁻⁵	4.0 ± 3.3	<5.4
NWA 4969	Ol	5	2.3 × 10 ⁻⁸	(0.345 ± 0.001) × 10 ⁻⁵	5.9 ± 3.2	5.9 ± 3.2
NWA 4969	Ol	5	2.2 × 10 ⁻⁸	(0.329 ± 0.002) × 10 ⁻⁵	5.5 ± 3.2	5.5 ± 3.2
NWA 4969	Ol	5	1.8 × 10 ⁻⁸	(0.326 ± 0.001) × 10 ⁻⁵	5.4 ± 3.2	5.4 ± 3.2
NWA 4969	Ol	5	1.6 × 10 ⁻⁸	(0.320 ± 0.001) × 10 ⁻⁵	5.3 ± 3.3	<5.4
NWA 4969	Ol	5	1.8 × 10 ⁻⁸	(0.295 ± 0.001) × 10 ⁻⁵	4.7 ± 3.3	<5.4
NWA 4969	Ol	5	1.4 × 10 ⁻⁸	(0.245 ± 0.001) × 10 ⁻⁵	3.4 ± 3.3	<5.4
NWA 4969	Ol	5	1.3 × 10 ⁻⁸	(0.244 ± 0.001) × 10 ⁻⁵	3.3 ± 3.3	<5.4
NWA 4969	Ol	5	1.2 × 10 ⁻⁸	(0.250 ± 0.001) × 10 ⁻⁵	3.5 ± 3.3	<5.4
NWA 4969	Ol	5	1.2 × 10 ⁻⁸	(0.252 ± 0.001) × 10 ⁻⁵	3.5 ± 3.3	<5.4
NWA 6693	Ol	5	2.2 × 10 ⁻⁸	(0.261 ± 0.001) × 10 ⁻⁵	3.8 ± 3.3	<5.4
NWA 6693	Ol	5	1.7 × 10 ⁻⁸	(0.244 ± 0.001) × 10 ⁻⁵	3.4 ± 3.3	<5.4
NWA 6693	Ol	5	2.2 × 10 ⁻⁸	(0.267 ± 0.002) × 10 ⁻⁵	3.9 ± 3.3	<5.4
NWA 6693	Ol	5	2.1 × 10 ⁻⁸	(0.307 ± 0.001) × 10 ⁻⁵	5.0 ± 3.3	<5.4
NWA 6693	OPx	4	1.9 × 10 ⁻⁸	(0.263 ± 0.001) × 10 ⁻⁵	2.2 ± 7.0	<6.9
NWA 6693	OPx	4	1.6 × 10 ⁻⁸	(0.268 ± 0.001) × 10 ⁻⁵	2.4 ± 7.0	<6.9
NWA 6693	OPx	4	1.5 × 10 ⁻⁸	(0.268 ± 0.001) × 10 ⁻⁵	2.3 ± 7.0	<6.9
NWA 7317	Ol	5	1.8 × 10 ⁻⁸	(0.240 ± 0.001) × 10 ⁻⁵	3.2 ± 3.3	<3.3
NWA 7317	Ol	5	1.5 × 10 ⁻⁸	(0.222 ± 0.001) × 10 ⁻⁵	2.8 ± 3.3	<3.3
NWA 7317	Ol	5	2.3 × 10 ⁻⁸	(0.232 ± 0.001) × 10 ⁻⁵	3.0 ± 3.3	<3.3
NWA 7317	Ol	5	2.3 × 10 ⁻⁸	(0.249 ± 0.001) × 10 ⁻⁵	3.5 ± 3.3	<5.4
NWA 7317	OPx	4	3.0 × 10 ⁻⁸	(0.287 ± 0.002) × 10 ⁻⁵	3.0 ± 7.0	<6.9
NWA 7317	OPx	4	2.7 × 10 ⁻⁸	(0.355 ± 0.002) × 10 ⁻⁵	5.3 ± 6.9	<6.9
NWA 7317	OPx	4	2.6 × 10 ⁻⁸	(0.250 ± 0.001) × 10 ⁻⁵	1.8 ± 7.0	<6.9
NWA 7317	OPx	4	2.8 × 10 ⁻⁸	(0.251 ± 0.001) × 10 ⁻⁵	1.8 ± 7.0	<6.9
NWA 7317	OPx	4	1.8 × 10 ⁻⁸	(0.299 ± 0.002) × 10 ⁻⁵	3.4 ± 7.0	<6.9
NWA 7317	OPx	4	2.0 × 10 ⁻⁸	(0.236 ± 0.001) × 10 ⁻⁵	1.3 ± 7.0	<6.9
NWA 7317	OPx	4	2.8 × 10 ⁻⁸	(0.234 ± 0.002) × 10 ⁻⁵	1.2 ± 7.0	<6.9

^a95.5% confidence intervals.^bFinal H₂O is the calculated H₂O content screened for the detection limits at 99.7% and 95.5% confidence, either stating the value (if above the 99.7% limit), the 99.7% upper limit (if above the 95.5% limit) or the 95.5% upper limit (if below).

chondrites. The LL parent body has been linked to the Flora asteroid family, for which a pre-disruptive diameter of its parent planetesimal of 150–220 km has been estimated (Brož et al., 2013; Vokrouhlický et al., 2017).

Recent size estimates by Pb-phosphate thermochronology suggest a minimum diameter of 300 km (Edwards & Blackburn, 2020). The latter corresponds to a pressure of ~322 bar in the body's center when assuming a bulk

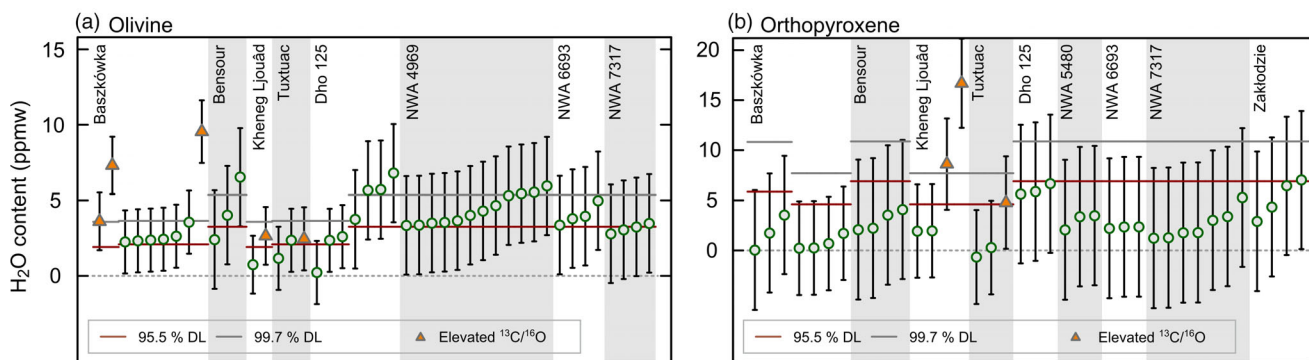


FIGURE 4. Summary of H_2O contents calculated from NanoSIMS $^1\text{H}/^{16}\text{O}$ ratios relative to the detection limits (DL). Error bars are 95.5% confidence intervals based on the uncertainty of the calibration parameters. Measurements with elevated $^{13}\text{C}/^{16}\text{O}$ ion ratios between 3×10^{-8} and 4.1×10^{-8} are marked and suspect of hydrocarbon contamination (those at $>4.1 \times 10^{-8}$ have been discarded, see text). Due to the calibration procedure, the instrumental (regressed) blank is at 0 ppmw H_2O . (a) Olivines. (b) Orthopyroxenes. (Color figure can be viewed at wileyonlinelibrary.com.)

density of 3200 kg m^{-3} . Metamorphic temperatures recorded by LL5-6 chondrites range between $\sim 800^\circ\text{C}$ (peak temperature) and $\sim 600^\circ\text{C}$ (closure of Mg-Fe interdiffusion). The H_2O fugacity was generally low due to low oxygen fugacity and high carbon activity recorded by the FeO contents of olivine and orthopyroxene coexisting with metallic Fe,Ni alloy and, in some cases, iron carbides. The fluid composition at near-peak metamorphism inferred from such equilibrium is rich in CH_4 and poor in H_2O (Harries & Langenhorst, 2018).

To assess the effect on the H_2O content of coexisting enstatite, we used the thermodynamic model of Harries and Langenhorst (2018) and the solubility relation of Mierdel and Keppler (2004) to calculate the equilibrium H_2O contents of enstatite coexisting with the metamorphic fluid at temperatures between 600 and 1000°C and pressures between 100 and 1000 bar (speciation as in fig. 6 of Harries & Langenhorst, 2018). Even under the most favorable conditions (high temperature, high pressure, buffered by graphite instead of carbide), the H_2O content of coexisting enstatite does not exceed 1.3 ppmw and is lower than 0.33 ppmw at 600– 800°C and pressures below 500 bar (Table 9).

The addition of Al_2O_3 increases H_2O solubility in enstatite due to charge-compensating coupled substitution (Rauch & Keppler, 2002), but the further addition of other trivalent cations such as Cr^{3+} can counteract this effect (Stalder et al., 2005). Al_2O_3 and Cr_2O_3 contents in orthopyroxenes of equilibrated LL chondrites are on the order of 0.17–0.25 wt% and 0.12–0.27 wt%, respectively (Brearley & Jones, 1998). Solubility experiments by Liu and Yang (2020) at oxygen fugacity of the iron-wüstite and Ni-NiO buffers using natural orthopyroxene ($\text{Fa}_{8.8-9.0}\text{Wo}_{0.2-0.3}$, 0.13–0.16 wt% Al_2O_3 and up to 0.02 wt% Cr_2O_3) differ from the H_2O contents predicted by the relation of Mierdel and Keppler (2004) by factors of

TABLE 9. Modeled H_2O contents of enstatite in LL chondrites.

Temperature ($^\circ\text{C}$)	Pressure (bar)	$f_{\text{H}_2\text{O}}$ (bar) ^a	$w_{\text{H}_2\text{O}}$ in OPx (ppmw)
600	100	1.1	0.03
600	500	2.7	0.06
600	1000	4.1	0.09
700	100	2.8	0.07
700	500	7.1	0.16
700	1000	11.0	0.23
800	100	5.6	0.13
800	500	15.4	0.33
800	1000	24.1	0.48
900	100	9.1	0.19
900	500	27.9	0.57
900	1000	44.5	0.85
1000	100	11.3	0.23
1000	500	43.3	0.85
1000	1000	71.6	1.33

^aFugacities calculated using the method of Harries and Langenhorst (2018).

about 0.5–5. Hence, even if Al_2O_3 would increase the H_2O solubility by a factor of a few (potentially compensated by additional Cr_2O_3 in LL orthopyroxenes), the resulting H_2O contents are still expected to be less than or similar to our NanoSIMS detection limits.

It seems unlikely that reduced hydrogen species such as CH_4 and H_2 would partition as hydroxyl defects into NAMs or would be incorporated as molecular species under the low pressures of planetesimal interiors (Moine et al., 2020; Yang et al., 2016). Hence, under equilibrium conditions, indicated by the thorough redistribution and homogenization of Mg and Fe in LL5-7 chondrites, hydrogen should have been almost entirely partitioned into an intergranular fluid phase (Dohmen et al., 1998) present along grain boundaries and within pores.

Extrapolating the above solubility calculation down to temperatures of 200°C results in H₂O contents of enstatite that are <15 ppmw in thermodynamic equilibrium, for example, ~10.5 ppmw at 300°C and ~12.6 ppmw H₂O at 200°C—even under the very optimistic assumption of a pure H₂O fluid at 322 bar ($P_{\text{H}_2\text{O}} = P_{\text{tot}}$). At such low temperatures, diffusion of oxygen-bound hydrogen into orthopyroxene becomes very slow. The hydrogen diffusion data of Stalder and Skogby (2003) indicate that a root mean squared displacement on the order of 100 μm (typical grain size of LL6 chondrites) by bulk diffusion takes about 76 ka at 300°C and more than 900 Ma at 200°C, effectively closing equilibration in-between those temperatures. Hence, even if a H₂O-rich fluid would have persisted over several hundred Ma, the resulting H₂O contents of orthopyroxene would be barely above our detection limits due to diffusive closure (when solubility is high below ~250°C) or limited solubility (when diffusivity is high above ~250°C).

H₂O in Chondrites and Itokawa Samples

The finding of several hundred ppmw H₂O in NAMs of equilibrated LL and L chondrites and Hayabusa-returned particles of asteroid Itokawa by Jin and Bose (2019) and Jin et al. (2021) are in contrast with our results and the above solubility considerations. The equilibrated LL5, LL5-6, and LL6 chondrites Tuxtuac, Kheneg Ljouâd, and Bensour studied here appear to be representative of typical highly equilibrated LL chondrites. This also appears to be the case for chondrites studied by Jin and Bose (2019) and Jin et al. (2021). Some of them, such as LAR 12036, have been classified into weathering category A/B or B, indicating minor to moderate staining by iron oxyhydroxides (Satterwhite & Righter, 2016), which is different from our samples Kheneg Ljouâd and Bensour, which do not show any discernible staining. Also, Jin et al. (2021) recognize elevated H₂O contents in NAMs of their Antarctic meteorite samples compared with the recent falls Chelyabinsk and Benenitra.

The Hayabusa samples studied by Jin and Bose (2019) and Chan et al. (2021) are certainly among the most pristine materials of this sort available, and it seems unlikely that terrestrial contamination or extraterrestrial ion implantation on the surface of 25143 Itokawa added significant amounts of hydrogen to the bulk pyroxenes grains. Secondary H₂O formation in the solar wind-implanted upper ~50–100 nm of common Itokawa regolith particles is expected (Daly et al., 2021), but this is strictly limited to grain surfaces. Jin and Bose (2019) state that the Hayabusa samples were embedded in epoxy and LAR 12036 was studied in the form of a standard polished thin section. We entirely avoided organic glues or resins in the final mounts as they are potential sources of surficial

hydrocarbon contamination. We cannot exclude intrinsic differences of our samples at this point, but it appears that we were able to largely avoid sample contamination, which allowed us to obtain very low background contributions and detection limits. On the other hand, Chan et al. (2021) confirmed elevated H₂O contents of 200–300 ppmw in olivine and orthopyroxene of a Hayabusa-returned regolith grain and detected ~1000 ppmw H₂O in coexisting albite. However, their sample contained significant amounts of extraterrestrial organic carbon and lower Fa and Fs components than typical LL-type Hayabusa samples, suggesting a late-stage addition of lowly equilibrated exogenous material to Itokawa's regolith. This leaves the possibility that heterogeneity exists among the Hayabusa regolith samples, including grains that did not experience strong thermal metamorphism and retain primary bulk H₂O contents. This appears to be unlikely in the case of the equilibrated LAR 12036.

In unequilibrated chondrites, Deloule et al. (1998) and Stephant et al. (2017) reported high H₂O contents in olivine (80–2100 ppmw), orthopyroxene (270–9800 ppmw), and mesostasis (4700–16,500 ppmw) of the Bishunpur LL3.1 and Semarkona LL3.00 chondrites. Shimizu et al. (2021) reported much lower H₂O contents of 9–14 ppmw in chondrule olivine and orthopyroxene of Semarkona and Queen Alexandra Range 97008 (LL3.05), but in some cases similar H₂O contents of chondrule mesostasis (up to 10200 ppmw). Shimizu et al. (2021) conclude that H₂O dissolution into the mesostasis occurred as a secondary process during processing within the parent body. The mesostasis H₂O contents suggest the presence of a hydrous fluid component during early, low-grade metamorphism.

In contrast, the above solubility considerations under high-grade metamorphic conditions indicate that multiple 10s or 100s of ppmw H₂O are unlikely in NAMs of highly equilibrated chondrites. Hence, not finding substantial H₂O in NAMs of equilibrated chondrites is consistent with equilibrium thermodynamics and diffusion kinetics. This (non-)observation is also corroborated by the very low H₂O contents of apatite in equilibrated LL chondrites (<96 ppmw; Jones et al., 2014), pointing to dry metamorphic fluids given apatite's affinity to structural incorporation of hydroxyl ions.

H₂O in Non-ordinary Chondrites and Achondrites

The primitive and differentiated achondrites and the CR6 chondrite NWA 7317 included in this survey are also essentially dry in terms of H₂O stored in olivine and orthopyroxene. Also, pyroxenes of eucrites, Angrites, and ureilites appear to be H₂O poor with upper limits of <13 ppmw H₂O determined by SIMS analysis (Dudley et al., 2018). Recent studies by Sarafian et al. (2019) and

Stephant et al. (2021) revealed 4–18 ppmw H₂O in clinopyroxenes of eucrites. Only the hydrogen-compatible apatite in eucrites contains appreciable amounts of H₂O on the order of 10s to a few 1000s ppmw (Barrett et al., 2016; Sarafian et al., 2014).

As outlined above, the incorporation of substantial amounts of H₂O into NAMs even in environments with high H₂O fugacity is controlled by pressure. In the interior of 4 Vesta, the expected pressure does not exceed ~1.2 kbar at the core–mantle boundary assuming a metallic core of 220 km diameter relative to the mean diameter of 525 km (Ermakov et al., 2014) and reasonable densities (3400 kg m⁻³ for the mantle, 7900 kg m⁻³ for the core). Although compared with the solar nebula Vesta's mantle is relatively oxidized with an oxygen fugacity about 2.2 log units below the iron-wüstite buffer (Righter & Drake, 1996), the molar H₂O/H₂ ratio is still expected to be on the order of 0.1 at about 1000°C. This temperature corresponds to roughly the lower temperature limit of {0k/}[100] pencil-glide slip systems that have been deemed responsible for the observed lattice-preferred orientation of olivine in NWA 5480 and that were used to infer Vestan mantle convection (Tkalcic et al., 2013). In the presence of such a H₂/H₂O fluid at 1.2 kbar and equilibration at 1000°C, the upper limit H₂O content of orthopyroxene would be on the order of 1–2 ppmw and less at shallower depth. Therefore, our non-detection of H₂O at a detection limit of 10.9 ppmw (99.7%) is consistent with a low mantle H₂O fugacity. Through mass balance, Stephant et al. (2021) estimated H₂O contents of Vesta's bulk silicate of 12–23 ppmw before extraction of basaltic melt, which suggests that the volatile H species were present dominantly as a fluid phase rather than as mineral-bound components, that is, the fluid-to-rock ratio was relatively high, while the actual H₂O fugacity was low. Hence, the migration of basaltic melts might have transported substantial amounts of hydrogen from the interiors of Vesta-like planetesimals to their surfaces.

The metal-bearing, FeO-rich lithologies studied here (NWA 4969, NWA 6693, NWA 7317) formed at oxygen fugacities comparable to or larger than that in LL chondritic meteorites given similar or higher Fa and Fs components in their olivine and pyroxene. Without constraints on the carbon activity, it is not viable to estimate the compositions of coexisting fluids, but the apparent absence of carbon-rich phases suggests that H₂O might have been a more dominant species compared with the LL mineralogy. However, this does not indicate that H₂O or any of the other fluid species was abundant in terms of a high fluid-to-rock ratio. The lack of substantial incorporation of hydrogen into the NAMs indicates that the pressure within the parent body was either too low for dissolving significant amounts of H₂O or that the abundance of hydrogen was low. If the parent

lithology in the cases of NWA 6693 and NWA 7317 was indeed a hydrated CR2-like chondrite as suggested by some isotopic constraints, the fluid released from phyllosilicates of the H₂O-rich protolith (~3.8–8.5 wt% bulk H₂O in CR2 chondrites; Weisberg et al., 1993) must have efficiently escaped from the parent planetesimal during or after metamorphism and magmatism.

CONCLUSIONS

Our survey of metamorphic chondrites and achondrites by NanoSIMS and FT-IR using careful, contamination-minimizing sample preparation shows the absence of detectable H₂O at levels larger than 10.9 ppmw in olivine and orthopyroxene. Our conservative approach to detection places the upper limits of H₂O even at lower contents in some cases and offers prospects to further improve low-level detection through better external calibration of reference materials.

The presence of only extremely small H₂O contents and the difficulty to detect them is not unexpected given the relatively small sizes of their parent planetesimals, which generated internal pressures much lower than those prevalent in the mantles of the terrestrial planets and the Moon. Although there is ample evidence that many primitive chondrites co-accreted hydrogen-bearing matter in the form of ice and organics, low pressures and reducing conditions led to speciation and low solubilities that prevented significant retention of volatiles by NAMs. The best record of the metamorphic or post-magmatic fluid phases probably exists in minerals that are much more compatible toward incorporation of volatiles, such as apatite (Barrett et al., 2016; Jones et al., 2014, 2016) or amphiboles (e.g., Floss et al., 2007; McCanta et al., 2008; Treiman & McCanta, 2010).

Our results show that olivine and orthopyroxene of highly equilibrated ordinary chondrites did not efficiently retain initially present hydrogen in the form of hydroxyl groups in their bulk crystal structures. During thermal metamorphism, the reduced volatile species resulting from initially several hundred ppmw H₂O in LL chondrites were probably predominantly present as an intergranular fluid phase as proposed by Dohmen et al. (1998). Such fluid potentially escaped much more efficiently due to fast diffusion along grain boundaries in contrast to the slow transport involving a large contribution of bulk diffusion as suggested by Jin and Bose (2019).

This small survey included metamorphic chondrites and achondrites from both the NC-like and CC-like reservoirs. In the cases of the CC-like materials—namely NWA 6693 and NWA 7317—it seems reasonable to assume that they accreted with at least some hydrous material even if they did not originate as CR2 chondrites *sensu stricto*. Under this assumption, hydrogen species

apparently escaped efficiently due to low pressure and high permeability.

Whether or not large, internally heated planetesimals could have efficiently delivered volatiles to the growing terrestrial planets cannot be answered comprehensively from the small set of samples studied here. However, there is indication that the physical and chemical conditions (low pressure, reduced hydrogen species) were often unfavorable for the structural retention of hydrogen in NAMs at metamorphic temperatures. The understanding of the processes involved requires additional and careful studies of how intergranular fluids behave during planetesimal evolution.

Acknowledgments—The NanoSIMS work was funded by a Europlanet transnational access grant (18-EPN4-064 to D.H.). Europlanet 2020 RI has received funding from the European Union's Horizon 2020 research and innovation program under grant agreement no. 654208. Reviews by Lydia Hallis and an anonymous reviewer are gratefully acknowledged. D.H. gratefully acknowledges the granting of access and support by Burkhard Schmidt at the FT-IR laboratory of the Department of Mineralogy at the Geoscience Center Göttingen. The SEM and Raman facilities at FSU Jena are supported by a DFG Gottfried Wilhelm Leibniz award to Falko Langenhorst (LA830/14-1). Open Access funding enabled and organized by Projekt DEAL.

Data Availability Statement—The data that support the findings of this study are available from the corresponding author upon reasonable request.

Editorial Handling—Dr. Kevin Righter

REFERENCES

- Agee, C. B., Aikin, H., and Ziegler, K. 2020. *Northwest Africa 12869: Primitive Achondrite from the CR2 Parent Body or Member of a New Meteorite Group?* 51st Lunar and Planetary Science Conference, abstract #2292.
- Alexander, C. M. O'D., McKeegan, K. D., and Altwegg, K. 2018. Water Reservoirs in Small Planetary Bodies: Meteorites, Asteroids, and Comets. *Space Science Reviews* 214: 36.
- Alexander, C. M. O'D., Barber, D. J., and Hutchison, R. 1989. The Microstructure of Semarkona and Bishunpur. *Geochimica et Cosmochimica Acta* 53: 3045–57.
- Barrett, T. J., Barnes, J. J., Tartèse, R., Anand, M., Franchi, I. A., Greenwood, R. C., Charlier, B. L. A., and Grady, M. M. 2016. The Abundance and Isotopic Composition of Water in Eucrites. *Meteoritics & Planetary Science* 51: 1110–24.
- Bell, D. R., Ihinger, P. D., and Rossman, G. R. 1995. Quantitative Analysis of Trace OH in Garnet and Pyroxenes. *American Mineralogist* 80: 465–74.
- Bell, D. R., Rossman, G. R., Maldener, J., Endisch, D., and Rauch, F. 2003. Hydroxide in Olivine: A Quantitative Determination of the Absolute Amount and Calibration of the IR Spectrum. *Journal of Geophysical Research: Solid Earth* 108: 2105.
- Brearley, A. J., and Jones, R. H. 1998. Chondritic Meteorites. *Reviews in Mineralogy and Geochemistry* 36: 3–398.
- Brož, M., Morbidelli, A., Bottke, W. F., Rozehnal, J., Vokrouhlický, D., and Nesvorný, D. 2013. Constraining the Cometary Flux through the Asteroid Belt during the Late Heavy Bombardment. *Astronomy & Astrophysics* 551: A117.
- Chan, Q. H. S., Stephant, A., Franchi, I. A., Zhao, X., Brunetto, R., Kebukawa, Y., Noguchi, T., et al. 2021. Organic Matter and Water from Asteroid Itokawa. *Scientific Reports* 11: 5125.
- Chennaoui, A. H., and Garvie, L. A. J. 2018. *Kheneg Ljouâd (Morocco): The Unique LL5/6 Meteorite Fall*. 81st Annual Meeting of the Meteoritical Society, abstract #6050.
- Connolly, H. C., Smith, C., Benedix, G., Folco, L., Righter, K., Zipfel, J., Yamaguchi, A., and Aoudjehane, H. C. 2007. The Meteoritical Bulletin, No. 92, 2007 September. *Meteoritics & Planetary Science* 42: 1647–94.
- Daly, L., Lee, M. R., Hallis, L. J., Ishii, H. A., Bradley, J. P., Bland, P. A., Saxey, D. W., et al. 2021. Solar Wind Contributions to Earth's Oceans. *Nature Astronomy* 5: 1275–85.
- Dauphas, N. 2017. The Isotopic Nature of the Earth's Accreting Material through Time. *Nature* 541: 521–4.
- Deloule, E., Robert, F., and Doukhan, J. C. 1998. Interstellar Hydroxyl in Meteoritic Chondrules: Implications for the Origin of Water in the Inner Solar System. *Geochimica et Cosmochimica Acta* 62: 3367–78.
- Dohmen, R., Chakraborty, S., Palme, H., and Rammensee, W. 1998. Solid-Solid Reactions Mediated by a Gas Phase: An Experimental Study of Reaction Progress and the Role of Surfaces in the System Olivine + Iron Metal. *American Mineralogist* 83: 970–84.
- Doyle, P. M., Jogo, K., Nagashima, K., Krot, A. N., Wakita, S., Ciesla, F. J., and Hutcheon, I. D. 2015. Early Aqueous Activity on the Ordinary and Carbonaceous Chondrite Parent Bodies Recorded by Fayalite. *Nature Communications* 6: 1–10.
- Dudley, J. M., Greenwood, J. P., Sakamoto, N., Abe, K., Kuroda, M., and Yurimoto, H. 2018. Water Contents of Angrites, Eucrites, and Ureilites, and New Methods for Measuring Hydrogen in Pyroxene Using SIMS. 49th Lunar and Planetary Science Conference, abstract #2223.
- Edwards, G. H., and Blackburn, T. 2020. Accretion of a Large LL Parent Planetesimal from a Recently Formed Chondrule Population. *Science Advances* 6: eaay8641.
- Ermakov, A. I., Zuber, M. T., Smith, D. E., Raymond, C. A., Balmino, G., Fu, R. R., and Ivanov, B. A. 2014. Constraints on Vesta's Interior Structure Using Gravity and Shape Models from the Dawn Mission. *Icarus* 240: 146–60.
- Floss, C. 2000. Complexities on the Acapulcoite-Lodranite Parent Body: Evidence from Trace Element Distributions in Silicate Minerals. *Meteoritics & Planetary Science* 35: 1073–85.
- Floss, C., Jolliff, B. L., Benedix, G. K., Stadermann, F. J., and Reid, J. 2007. Hammadah al Hamra 193: The First Amphibole-Bearing Winonaite. *American Mineralogist* 92: 460–7.
- Gardner-Vandy, K. G., Lauretta, D. S., Greenwood, R. C., McCoy, T. J., Killgore, M., and Franchi, I. A. 2012. The Tafassasset Primitive Achondrite: Insights into Initial Stages of Planetary Differentiation. *Geochimica et Cosmochimica Acta* 85: 142–59.

- Garvie, L. A. J. 2012. The Meteoritical Bulletin, No. 99, April 2012. *Meteoritics & Planetary Science* 47: E1–52.
- Gattacceca, J., Rochette, P., and Bourot-Denise, M. 2003. Magnetic Properties of a Freshly Fallen LL Ordinary Chondrite: The Bensour Meteorite. *Physics of the Earth and Planetary Interiors* 140: 343–58.
- Graham, A. L., Michel-Levy, M. C., Danon, J., and Easton, A. J. 1988. The Tuxtuac, Mexico, Meteorite, an LL5 Chondrite Fall. *Meteoritics* 23: 321–3.
- Grossman, J. N., Alexander, C. M. O'D., Wang, J., and Brearley, A. J. 2000. Bleached Chondrules: Evidence for Widespread Aqueous Processes on the Parent Asteroids of Ordinary Chondrites. *Meteoritics & Planetary Science* 35: 467–86.
- Grossman, J. N., and Zipfel, J. 2001. The Meteoritical Bulletin, No. 85, 2001 September. *Meteoritics & Planetary Science* 36: A293–322.
- Harries, D., and Langenhorst, F. 2018. Carbide-Metal Assemblages in a Sample Returned from Asteroid 25143 Itokawa: Evidence for Methane-Rich Fluids during Metamorphism. *Geochimica et Cosmochimica Acta* 222: 53–73.
- Hibiya, Y., Archer, G. J., Tanaka, R., Sanborn, M. E., Sato, Y., Iizuka, T., Ozawa, K., et al. 2019. The Origin of the Unique Achondrite Northwest Africa 6704: Constraints from Petrology, Chemistry and Re–Os, O and Ti Isotope Systematics. *Geochimica et Cosmochimica Acta* 245: 597–627.
- Hoppe, P., Cohen, S., and Meibom, A. 2013. NanoSIMS: Technical Aspects and Applications in Cosmochemistry and Biological Geochemistry. *Geostandards and Geoanalytical Research* 37: 111–54.
- Hutchison, R., Alexander, C. M. O'D., and Barber, D. J. 1987. The Semarkona Meteorite: First Recorded Occurrence of Smectite in an Ordinary Chondrite, and its Implications. *Geochimica et Cosmochimica Acta* 51: 1875–82.
- Jin, Z., and Bose, M. 2019. New Clues to Ancient Water on Itokawa. *Science Advances* 5: eaav8106.
- Jin, Z., Bose, M., Lichtenberg, T., and Mulders, G. D. 2021. New Evidence for Wet Accretion of Inner Solar System Planetesimals from Meteorites Chelyabinsk and Benenitra. *The Planetary Science Journal* 2: 244.
- Jones, R. H., McCubbin, F. M., Dreeland, L., Guan, Y., Burger, P. V., and Shearer, C. K. 2014. Phosphate Minerals in LL Chondrites: A Record of the Action of Fluids during Metamorphism on Ordinary Chondrite Parent Bodies. *Geochimica et Cosmochimica Acta* 132: 120–40.
- Jones, R. H., McCubbin, F. M., and Guan, Y. 2016. Phosphate Minerals in the H Group of Ordinary Chondrites, and Fluid Activity Recorded by Apatite Heterogeneity in the Zag H3-6 Regolith Breccia. *American Mineralogist* 101: 2452–67.
- Keil, K. 2010. Enstatite Achondrite Meteorites (Aubrites) and the Histories of their Asteroidal Parent Bodies. *Geochemistry* 70: 295–317.
- Keil, K. 2014. Brachinite Meteorites: Partial Melt Residues from an FeO-Rich Asteroid. *Geochemistry* 74: 311–29.
- Krzesińska, A. M., and Almeida, N. V. 2019. Evidence of Shock-Induced Vaporization of Matrix to Form Porosity in Baszkówka, a Porous L5 Chondrite. *Meteoritics & Planetary Science* 54: 54–71.
- Lemaire, C., Kohn, S. C., and Brooker, R. A. 2004. The Effect of Silica Activity on the Incorporation Mechanisms of Water in Synthetic Forsterite: A Polarised Infrared Spectroscopic Study. *Contributions to Mineralogy and Petrology* 147: 48–57.
- Liland, K. H., Almøy, T., and Mevik, B.-H. 2010. Optimal Choice of Baseline Correction for Multivariate Calibration of Spectra. *Applied Spectroscopy* 64: 1007–16.
- Liu, H., and Yang, X. 2020. Solubility of Hydroxyl Groups in Pyroxenes: Effect of Oxygen Fugacity at 0.2–3 GPa and 800–1200 °C. *Geochimica et Cosmochimica Acta* 286: 355–79.
- Mamtani, M. A., Chakraborty, R., Biswas, S., Suryawanshi, A., Goswami, S., and Bhatt, S. 2020. SEM-EBSD Analysis of Broad Ion Beam Polished Rock Thin Sections—The MFAL Protocol. *Journal of the Geological Society of India* 95: 337–42.
- Matsumoto, T., Tsuchiyama, A., Uesugi, K., Nakano, T., Uesugi, M., Matsuno, J., Nagano, T., et al. 2016. Nanomorphology of Itokawa Regolith Particles: Application to Space-Weathering Processes Affecting the Itokawa Asteroid. *Geochimica et Cosmochimica Acta* 187: 195–217.
- McCanta, M. C., Treiman, A. H., Dyar, M. D., Alexander, C. M. O'D., Rumble, D., and Essene, E. J. 2008. The LaPaz Icefield 04840 Meteorite: Mineralogy, Metamorphism, and Origin of an Amphibole- and Biotite-Bearing R Chondrite. *Geochimica et Cosmochimica Acta* 72: 5757–80.
- McCoy, T. J., Corrigan, C. M., Dickinson, T. L., Benedix, G. K., Schrader, D. L., and Davidson, J. 2019. Grove Mountains (GRV) 020043: Insights into Acapulcoite-Lodranite Genesis from the most Primitive Member. *Geochemistry* 79: 125536.
- Mierdel, K., and Keppler, H. 2004. The Temperature Dependence of Water Solubility in Enstatite. *Contributions to Mineralogy and Petrology* 148: 305–11.
- Moine, B. N., Bolfan-Casanova, N., Radu, I. B., Ionov, D. A., Costin, G., Korsakov, A. V., Golovin, A. V., Oleinikov, O. B., Deloule, E., and Cottin, J. Y. 2020. Molecular Hydrogen in Minerals as a Clue to Interpret δD Variations in the Mantle. *Nature Communications* 11: 3604.
- Morbidelli, A., Bottke, W. F., Nesvorný, D., and Levison, H. F. 2009. Asteroids Were Born Big. *Icarus* 204: 558–73.
- Nakamura, T., Noguchi, T., Tanaka, M., Zolensky, M. E., Kimura, M., Tsuchiyama, A., Nakato, A., et al. 2011. Itokawa Dust Particles: A Direct Link between S-Type Asteroids and Ordinary Chondrites. *Science* 333: 1113–6.
- Patzer, A., Hill, D. H., and Boynton, W. V. 2004. Evolution and Classification of Acapulcoites and Lodranites from a Chemical Point of View. *Meteoritics & Planetary Science* 39: 61–85.
- Peslier, A. H. 2010. A Review of Water Contents of Nominally Anhydrous Natural Minerals in the Mantles of Earth, Mars and the Moon. *Journal of Volcanology and Geothermal Research* 197: 239–58.
- Piani, L., Marrocchi, Y., Rigaudier, T., Vacher, L. G., Thomassin, D., and Marty, B. 2020. Earth's Water may have been Inherited from Material Similar to Enstatite Chondrite Meteorites. *Science* 369: 1110–3.
- Przylibski, T. A., Zagożdżon, P. P., Kryza, R., and Pilski, A. S. 2005. The Zakłodzie Enstatite Meteorite: Mineralogy, Petrology, Origin, and Classification. *Meteoritics & Planetary Science* 40: A185–200.
- Rauch, M., and Keppler, H. 2002. Water Solubility in Orthopyroxene. *Contributions to Mineralogy and Petrology* 143: 525–36.

- Raymond, S. N., and Morbidelli, A. 2014. The Grand Tack Model: A Critical Review. *Proceedings of the International Astronomical Union* 9: 194–203.
- Righter, K., and Drake, M. J. 1996. Core Formation in Earth's Moon, Mars, and Vesta. *Icarus* 124: 513–29.
- Rubie, D. C., Frost, D. J., Mann, U., Asahara, Y., Nimmo, F., Tsuno, K., Kegler, P., Holzheid, A., and Palme, H. 2011. Heterogeneous Accretion, Composition and Core–Mantle Differentiation of the Earth. *Earth and Planetary Science Letters* 301: 31–42.
- Rubie, D. C., Jacobson, S. A., Morbidelli, A., O'Brien, D. P., Young, E. D., de Vries, J., Nimmo, F., Palme, H., and Frost, D. J. 2015. Accretion and Differentiation of the Terrestrial Planets with Implications for the Compositions of Early-Formed Solar System Bodies and Accretion of Water. *Icarus* 248: 89–108.
- Ruzicka, A., Grossman, J., Bouvier, A., Herd, C. D. K., and Agee, C. B. 2015. The Meteoritical Bulletin, No. 102. *Meteoritics & Planetary Science* 50: 1662–2.
- Sanborn, M. E., Wimpenny, J., Williams, C. D., Yamakawa, A., Amelin, Y., Irving, A. J., and Yin, Q.-Z. 2019. Carbonaceous Achondrites Northwest Africa 6704/6693: Milestones for Early Solar System Chronology and Genealogy. *Geochimica et Cosmochimica Acta* 245: 577–96.
- Sarafian, A. R., Nielsen, S. G., Marschall, H. R., Gaetani, G. A., Righter, K., and Berger, E. L. 2019. The Water and Fluorine Content of 4 Vesta. *Geochimica et Cosmochimica Acta* 266: 568–81.
- Sarafian, A. R., Nielsen, S. G., Marschall, H. R., McCubbin, F. M., and Monteleone, B. D. 2014. Early Accretion of Water in the Inner Solar System from a Carbonaceous Chondrite–Like Source. *Science* 346: 623–6.
- Satterwhite, C., and Righter, K. 2016. *Antarctic Meteorite Newsletter* 39: 1–33.
- Shimizu, K., Alexander, C. M. O'D., Hauri, E. H., Sarafian, A. R., Nittler, L. R., Wang, J., Jacobsen, S. D., and Mendybaev, R. A. 2021. Highly Volatile Element (H, C, F, Cl, S) Abundances and H Isotopic Compositions in Chondrules from Carbonaceous and Ordinary Chondrites. *Geochimica et Cosmochimica Acta* 301: 230–58.
- Stalder, R., Klemme, S., Ludwig, T., and Skogby, H. 2005. Hydrogen Incorporation in Orthopyroxene: Interaction of Different Trivalent Cations. *Contributions to Mineralogy and Petrology* 150: 473–85.
- Stalder, R., and Ludwig, T. 2007. OH Incorporation in Synthetic Diopside. *European Journal of Mineralogy* 19: 373–80.
- Stalder, R., Prechtel, F., and Ludwig, T. 2012. No Site-Specific Infrared Absorption Coefficients for OH-Defects in Pure Enstatite. *European Journal of Mineralogy* 24: 465–70.
- Stalder, R., and Skogby, H. 2003. Hydrogen Diffusion in Natural and Synthetic Orthopyroxene. *Physics and Chemistry of Minerals* 30: 12–9.
- Stephant, A., Remusat, L., and Robert, F. 2017. Water in Type I Chondrules of Paris CM Chondrite. *Geochimica et Cosmochimica Acta* 199: 75–90.
- Stephant, A., Wadhwa, M., Hervig, R., Bose, M., Zhao, X., Barrett, T. J., Anand, M., and Franchi, I. A. 2021. A Deuterium-Poor Water Reservoir in the Asteroid 4 Vesta and the Inner Solar System. *Geochimica et Cosmochimica Acta* 297: 203–19.
- Tkalcec, B. J., and Brenker, F. E. 2015. Asteroidal Processes Recorded by Polyphase Deformation in a Harzburgitic Diogenite NWA 5480. *Journal of Structural Geology* 77: 138–50.
- Tkalcec, B. J., Golabek, G. J., and Brenker, F. E. 2013. Solid-State Plastic Deformation in the Dynamic Interior of a Differentiated Asteroid. *Nature Geoscience* 6: 93–7.
- Treiman, A. H., and McCanta, M. C. 2010. Amphibole-Rich R Chondrite LAP 04840—From an Icy Asteroid or Main-Belt Comet? 73rd Annual Meeting of the Meteoritical Society, abstract #5389.
- Vokrouhlický, D., Bottke, W. F., and Nesvorný, D. 2017. Forming the Flora Family: Implications for the Near-Earth Asteroid Population and Large Terrestrial Planet Impactors. *The Astronomical Journal* 153: 172.
- Walsh, K. J., Morbidelli, A., Raymond, S. N., O'Brien, D. P., and Mandell, A. M. 2011. A Low Mass for Mars from Jupiter's Early Gas-Driven Migration. *Nature* 475: 206–9.
- Warren, P. H. 2011. Stable-Isotopic Anomalies and the Accretionary Assemblage of the Earth and Mars: A Subordinate Role for Carbonaceous Chondrites. *Earth and Planetary Science Letters* 311: 93–100.
- Warren, P. H., Rubin, A. E., Isa, J., Brittenham, S., Ahn, I., and Choi, B.-G. 2013. Northwest Africa 6693: A New Type of FeO-Rich, Low- $\Delta^{17}\text{O}$, Poikilitic Cumulate Achondrite. *Geochimica et Cosmochimica Acta* 107: 135–54.
- Weisberg, M. K., Prinz, M., Clayton, R. N., and Mayeda, T. K. 1993. The CR (Renazzo-Type) Carbonaceous Chondrite Group and its Implications. *Geochimica et Cosmochimica Acta* 57: 1567–86.
- Weisberg, M. K., Smith, C., Benedix, G., Folco, L., Righter, K., Zipfel, J., Yamaguchi, A., and Aoudjehane, H. C. 2009. The Meteoritical Bulletin, No. 95. *Meteoritics & Planetary Science* 44: 429–62.
- Withers, A. C., Bureau, H., Raepsaet, C., and Hirschmann, M. M. 2012. Calibration of Infrared Spectroscopy by Elastic Recoil Detection Analysis of H in Synthetic Olivine. *Chemical Geology* 334: 92–8.
- Wlotzka, F. 1993. A Weathering Scale for the Ordinary Chondrites. *Meteoritics* 28: 460.
- Wlotzka, F., and Otto, J. 2012. Euhedral Crystals in Interstitial Pores of the Baszkówka and Mt. Tazerzait L5 Chondrites. *Geological Quarterly* 45: 257–62.
- Yang, X., Keppler, H., and Li, Y. 2016. Molecular Hydrogen in Mantle Minerals. *Geochemical Perspectives Letters* 2: 160–8.
- Zipfel, J., Bischoff, A., Schultz, L., Spettel, B., Dreibus, G., Schönbeck, T., and Palme, H. 2010. Mineralogy, Chemistry, and Irradiation Record of Neuschwanstein (EL6) Chondrite. *Meteoritics & Planetary Science* 45: 1488–501.

SUPPORTING INFORMATION

Additional supporting information may be found in the online version of this article.

Data S1. Supplementary figures S1–S7, supplementary tables S1 and S2.